Available online at www.sciencedirect.com
ScienceDirect
Solid State Ionics 177 (2006) 2013–2021
SOLID STATE IONICS
www.elsevier.com/locate/ssi

Recent advances in single-chamber fuel-cells: Experiment and modeling

Yong Hao [a], Zongping Shao [b], Jennifer Mederos [b], Wei Lai [b], David G. Goodwin [a], Sossina M. Haile [b,*]

[a] *Mechanical Engineering, California Institute of Technology, Pasadena, California 91125, USA*
[b] *Materials Science, California Institute of Technology, Pasadena, California 91125, USA*

Received 16 January 2006; received in revised form 6 May 2006; accepted 6 May 2006

Abstract

Single-chamber fuel cells (SCFC) are ones in which the fuel and oxidizer are premixed, and selective electrode catalysts are used to generate the oxygen partial pressure gradient that in a conventional dual-chamber design is produced by physical separation of the fuel and oxidizer streams. SCFCs have been shown capable of generating power densities above 700 mW/cm^2 with appropriate catalysts, making them potentially useful in many applications where the simplicity of a single gas chamber and absence of seals offsets the expected lower efficiency of SCFCs compared to dual-chamber SOFCs.

SCFC performance is found to depend sensitively on cell microstructure, geometry, and flow conditions, making experimental optimization tedious. In this paper, we describe recent work focused on developing a quantitative understanding the physical processes responsible for SCFC performance, and the development of an experimentally-validated, physically-based numerical model to allow more rational design and optimization of SCFCs. The use of the model to explore the effects of fuel/oxidizer ratio, anode thickness, and flow configuration is discussed.

Keywords: Solid oxide fuel cell; Single chamber; Hydrocarbon fuels; Experiment and simulation

1. Introduction

While solid oxide fuel cells (SOFCs) exhibit a number of attractive features for power generation, including high energy conversion efficiency, fuel flexibility and relatively inexpensive electrode materials, the high temperatures required for operation (800–1000 °C) introduce a number of challenges. In particular, for planar SOFCs, thermal expansion mismatches between components can lead to failure of the seals that separate anode and cathode chambers. One strategy for addressing this challenge is to utilize so-called 'single chamber fuel cells' (SCFCs) in which the fuel and oxidant are allowed to mix and anode and cathode reactions take place within the same physical chamber [1].

The functionality of SCFCs derives from the selectivity of the electrode catalysts, with the anode preferentially oxidizing the fuel and the cathode preferentially reducing oxygen. The resulting oxygen partial pressure gradient generated across the cell in turn generates an electrical potential gradient. Useful power outputs are typically obtained under fuel rich conditions relative to complete oxidation [1–3]. Although the power density and efficiency are typically lower than those of conventional dual-chamber SOFCs (as a consequence of incomplete fuel utilization and parasitic, non-electrochemical fuel oxidation), the latest advances in materials science and system design have greatly improved SCFC power densities, in part, by lowering the fuel cell operating temperature so as to minimize purely chemical oxidation of the fuel [2,3].

Despite the lower efficiency, SCFCs have advantages over dual-chamber SOFCs that are particularly relevant for portable power generation. Because complications due to sealing are eliminated, the SCFC greatly simplifies the system design and enhances the thermal and mechanical shock resistance, thereby enabling rapid start up and shut down. The relatively low temperatures (400–600 °C) at which the most advanced SCFCs function also help to ease complications with on–off cycling. The reduced temperatures of operation provide additional benefits including expanding the choices of materials for fabrication of peripheral components and inhibiting carbon deposition via hydrocarbon cracking at the anode catalyst. Quite significantly, micro-SCFC systems can be designed

* Corresponding author. Fax: +1 626 395 3933.
E-mail address: smhaile@caltech.edu (S.M. Haile).

0167-2738/$ - see front matter © 2006 Elsevier B.V. All rights reserved.
doi:10.1016/j.ssi.2006.05.008

to be thermally self-sustaining [3] (such that no external heat source is required for fuel cell operation), a particularly important feature for portable applications.

To date, SCFC development has proceeded primarily via experimental optimization of the multiple parameters relevant to the power output. These efforts have yielded impressive results; indeed, using methane, ethane and propane fuels, respectively, peak power densities of ~650 [2,4], ~400 [1] and ~440 mW/cm^2 [5] have been reported in the literature. However, the extreme sensitivity of SCFC performance to variations in cell microstructure (resulting from variations in cell fabrication methods), chamber geometry, and flow conditions [6] renders a computational strategy for optimizing power output highly attractive. Accordingly, we report here a combined experimental and numerical simulation effort to simultaneously continue materials development for enhancing power output and to comprehensively describe the fundamental principles that dictate the cell performance, design tradeoffs and system optimization.

2. Fabrication and operation of single chamber fuel cells

The physical arrangement of a typical single chamber fuel cell utilized in this work is shown in Fig. 1. Samaria-doped ceria ($Sm_{0.15}Ce_{0.8}O_{1.925}$, SDC) serves as the electrolyte, Ni+SDC as the anode (SDC:NiO=40:60 by wt), and a mixture of $Ba_{0.5}Sr_{0.5}Co_{0.8}Fe_{0.2}O_{3-\delta}$+SDC (70:30 by wt) as the cathode. The anode-supported structures were fabricated with a diameter of 1.33 cm, and anode, electrolyte and cathode thickness of 700 μm, 15 μm and 10 μm, respectively, by a procedure described in detail elsewhere [5,6]. The cathode active area (used for the conversion of absolute current to current density) was 0.71 cm^2.

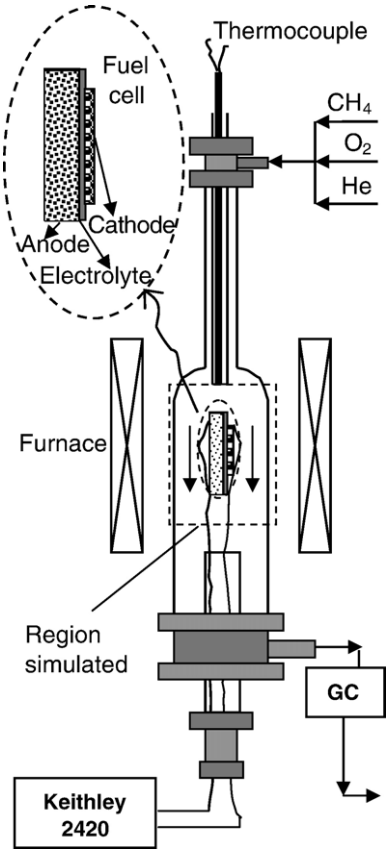

Fig. 1. Experimental configuration employed for measuring the voltage–current characteristics of single chamber fuel cells.

The premixed gas stream (oxygen+methane+helium) was supplied through the top of the reactor (inner diameter of 1.59 cm) and the cells were placed parallel to the streamwise direction. Within the porous anode, partial oxidation of methane fuel to yield CO and H_2 occurs, releasing significant heat, followed by electro-oxidation of the fuel at the anode–electrolyte interface. As in a conventional fuel cell, electro-reduction of oxygen occurs at the cathode–electrolyte interface and oxygen ions are transported across the electrolyte. In addition, within the porous cathode, undesirable oxidation of the methane fuel can also occur, as does undesirable electronic transport across the ceria electrolyte.

Fuel cell polarization curves were obtained at furnace temperatures of 500 to 650 °C, and for gas compositions in which the methane flow rate was fixed at 87 sccm, the oxygen to helium ratio fixed at 1:4, and the oxygen flow rate varied from 70 to 90 sccm. In addition to the current–voltage characteristics, the actual cell temperature was measured using a thermocouple placed in contact with the fuel cell anode (in some cases at multiple positions on the anode).

3. The numerical model

The complexity of the situation illustrated in Fig. 1 requires that several submodels, each developed on the basis of first principles and experimental input, be utilized and appropriately coupled to describe the complete fuel cell system. The individual submodels employed describe (1) gas flow characteristics surrounding the fuel cell, (2) chemical reaction and transport within the porous electrodes, (3) heat generation and transfer, (4) electrochemical reaction at the electrode–electrolyte interfaces, and (5) mixed ionic and electronic conductivity of the ceria electrolyte. The reader is referred to our previous work [7] for full details of the model development. In the present paper, we give a brief review of this two-dimensional model and place emphasis on the calibration of the model by experimental data and on the prediction of fuel cell performance beyond the experimental measurement regime.

The gas flow submodel solves the equations for the conservation of mass, momentum and energy to determine the two-dimensional distributions of velocity, density, temperature and gas-phase species in the gas chamber surrounding the fuel cell. It allows deployment of multiple cells in one chamber, with each cell either perpendicular or parallel to the streamwise direction. Simulation of a single cell can be either isothermal or non-isothermal, while that of multiple cells is isothermal only. Fluid properties are computed using the CANTERA software package [7].

The submodel for porous media transport and reaction employs the Dusty-Gas Model (DGM) [8] for species transport in both electrodes. This formalism accounts for all the major mechanisms for gaseous molecular transport in porous media including bulk molecular diffusion, Knudson diffusion and Darcy flow. To treat the consumption and generation of species due to heterogeneous reaction, detailed chemical information is

required. In the case of the anode, an experimentally verified partial oxidation mechanism of methane over Ni [9] was employed. In contrast, no analogous mechanism for the catalytic oxidation of methane over the cathode, BSCF, is available in the literature. Accordingly, a set of experiments were carried out with the objective of parametrizing the reaction process, without necessarily developing a detailed mechanistic understanding of the reaction pathway. The experiments and results are described below. Oxidation of CO and H_2 on the cathode surface was taken to be infinitely fast. Parameters describing the physical state of the electrodes (porosity, surface area, etc.) were taken from experimental measurements (electron microscopy, BET surface area analysis, etc.) of complete fuel cell structures.

The heat transfer submodel is based on the overall energy balance of the fuel cell. It considers heat conduction within the MEA, enthalpy changes at the electrodes, joule heating due to electrolyte resistance, and thermal radiation heat exchange between the MEA and furnace in the case of a single cell. Convection is also taken into account by coupling this module with the gas flow submodel through appropriate boundary conditions. The temperature distribution within the fuel cell is assumed to be 1-D along the x (streamwise) direction (i.e., uniform along the perpendicular direction). Gas enthalpies are calculated using the CANTERA package [7]. The emissivity and thermal conductivity of the fuel cell, being unavailable from the literature, are obtained as described below. This submodel is enabled only for non-isothermal simulations. Realistic simulation of thermal effects is essential for predicting fuel cell behavior, because temperature rises as great as 100–200 °C beyond the furnace temperature are experimentally observed [5,10,11].

The submodel for describing the fuel cell electrochemical behavior computes the local ionic current density $i(x)$ given the specified load potential E (assumed to be uniform along the cell) by solving the equation

$$E = E_0 - \frac{L_e i}{\sigma_i(T) A} - \eta_{\mathrm{act,a}}(i) - \eta_{\mathrm{act,c}}(i) \tag{1}$$

Here E_0 is the Nernst potential, L_e is the electrolyte thickness, A is the electrolyte area, $\sigma_i(T)$ is the electrolyte ionic conductivity, and $\eta_{\mathrm{act,a}}(i)$ and $\eta_{\mathrm{act,c}}(i)$ are the anode and cathode activation overpotentials, respectively. The variation in ionic current density with location along the length of the fuel cell is explicitly treated. The influence of the electronic current flow is treated subsequent to this initial computation, as described below.

Some care must be taken in computing the Nernst potential, since this depends on the gas composition. The relevant composition is the *actual* gas composition at the electrode/electrolyte interface, which, particularly in the anode, differs greatly from the incoming fuel composition, due to partial oxidation. We assume that the electrochemically-active species at the anode is hydrogen, and compute the Nernst potential as

$$E_0 = -\frac{\Delta G^0}{2F} + \frac{RT}{2F} \ln \frac{P_{\mathrm{H_2}} P_{\mathrm{O_2}}^{1/2}}{P_{\mathrm{H_2O}}} \tag{2}$$

where ΔG^0 is the standard free energy of the reaction $H_2 + \frac{1}{2} O_2 \rightleftharpoons H_2O$, and the partial pressures are evaluated at the anode/electrolyte interface for H_2 and H_2O, and at the cathode/electrolyte interface for O_2. Direct evaluation of E_0 via Eq. (2) is possible, since the model fully resolves the profiles of gaseous species through the thickness of the anode (and cathode), accounting for the coupled effects of finite-rate porous media transport, fuel depletion in the gas, and catalytic chemistry within the electrode (e.g. partial oxidation). Because the partial pressures are evaluated at the electrochemically-active region near the electrolyte, these effects are automatically accounted for in Eq. (1), without requiring an explicit concentration overpotential term. (Indeed, since H_2 is generated in situ, and is not present in the incoming fuel stream, no formulation in terms of a conventional concentration overpotential is possible.)

Although H_2 and CO are both electrochemically active fuels, here we neglect direct electrochemical oxidation of CO. Carbon monoxide is, however, indirectly oxidized by the rapid water–gas-shift reaction

$$CO + H_2O \rightleftharpoons CO_2 + H_2 \tag{3}$$

that proceeds in the net forward direction to replenish the H_2 depleted by electrochemical oxidation. The overall effect is that CO in the anode is oxidized to CO_2 at the same time as H_2 is oxidized to H_2O. Since in practice the reactions are sufficiently fast so as to maintain a low CO concentration at the anode (as shown by the simulations), including *direct* electrochemical oxidation of CO would not substantially alter the results.

The electrode activation overpotentials are evaluated by (numerically) inverting the Butler–Volmer equation

$$i = i_0 \left[\exp\left(\frac{\alpha_a \eta F}{RT}\right) - \exp\left(\frac{-\alpha_c \eta F}{RT}\right) \right] \tag{4}$$

at the anode– and cathode–electrolyte interfaces, respectively, where i_0 is the exchange current density, α_a and α_c are, respectively, the anodic and cathodic asymmetry factors, F is Faraday's constant, and R is the universal gas constant; i is again the ionic current density. Thus, three parameters, i_0, α_a, and α_c, must be determined for each of the two electrodes. The procedures and results used to obtain values for these parameters are described below.

The submodel for describing the electronic current through the ceria electrolyte is based on a model developed by Riess, Gödickemeier, and Gauckler [12–15]. In a typical experimental situation, one has knowledge of the gas phase oxygen partial pressures in separate anode and cathode chambers, and evaluation of the current–voltage characteristics of the cell are complicated by the unknown drops in chemical potential across the electrodes, which are convoluted with the unknown value of electronic current density. Here, the situation is substantially simpler because the gas concentrations at the electrode–electrolyte interfaces can be directly obtained from the solution of the porous electrode model. The electronic current is then directly computed using the relationship

$$i_e = -i \frac{\sigma_e(p_{\mathrm{O_2}}^{\mathrm{c}})}{\sigma_i} e^{\eta_c F/RT} \left(\frac{e^{EF/RT} - 1}{1 - e^{-iL_eF/RTA\sigma_i}} \right) \tag{5}$$

where $\sigma_e(p_{\mathrm{O_2}}{}^{\mathrm{c}})$ is the electronic conductivity evaluated at $p_{\mathrm{O_2}}{}^{\mathrm{c}}$, the oxygen partial pressure at the cathode–electrolyte interface, σ_i

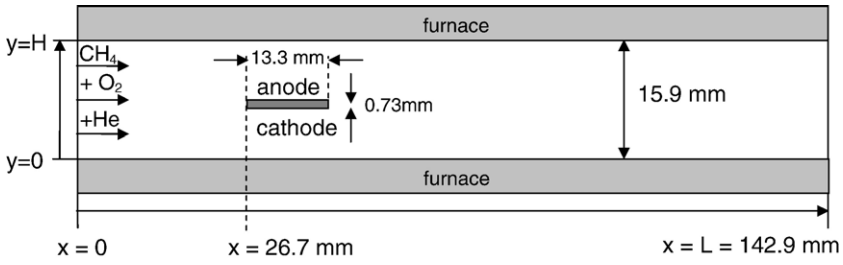

Fig. 2. Computational domain corresponding to the experimental configuration of Fig. 1.

is the ionic conductivity, and the remaining terms have been previously defined. The electronic and ionic transport properties of the ceria used here have been fully characterized, with the results reported in [16]. The electronic conductivity depends on both oxygen partial pressure and temperature according to

$$\sigma_e = \frac{k_e}{T}\exp\left(\frac{-E_e}{k_b T}\right)p_{O_2}^{-1/4} \quad (6)$$

with $k_e = 2.42\times10^8$ K Ω^{-1} cm^{-1} atm$^{1/4}$ and $E_e = 2.31\pm0.02$ eV, whereas the ionic conductivity depends only on temperature, with a pre-exponential term of 1.15×10^5 K Ω^{-1} cm^{-1} and an activation energy of 0.67 ± 0.01 eV.

The computation of the electronic current is decoupled from the remainder of the model, and is only required in order to evaluate the total current density $i_{tot} = i + i_e$, which corresponds to the experimentally measured current density. Since the electronic and ionic currents have opposite sign, at open circuit ($i_{tot} = 0$), both the ionic current i and the electronic current i_e are non-zero; for this reason, the measured open-circuit potential is lower than the value that would be expected for purely ionic conductor.

In correspondence with the experimental configuration of Fig. 1, the computation domain of the two-dimensional model, Fig. 2, is taken as the cross-sectional rectangular region within the tube furnace that contains the fuel cell. All relevant dimensions in the computation are set to be equal to those of the experiment (reactor diameter, fuel cell dimensions, etc.). The fuel cell power output was found, through both experiment and simulation, to be insensitive to the effects of gravity and hence the choice of orientation of the reactor (vertical vs. horizontal) has negligible (less that 0.5%) influence on the results. In the horizontally oriented computation domain, the gas enters as $x = 0$ and the leading edge of the fuel cell is placed at $x = 26.7$ mm.

Table 1
Selected parameters describing the structure and properties of SCFC fabricated and simulated in this study

Parameters	Value	Units
Anode: Ni+$Ce_{0.85}Sm_{0.15}O_{2-\delta}$		
Thickness	700	μm
Porosity	0.5	–
Tortuosity	3.6	–
Average pore radius	0.4	μm
Average particle diameter	1.0	μm
Specific catalyst area	7×10^5	m^2/m^3
α_a	1.0	–
α_c	0.4	–
Cathode:		
Thickness	10	μm
Porosity	0.3	–
Tortuosity	1.0	–
Average pore radius	0.4	μm
Average particle diameter	1.0	μm
Specific catalyst area	1.06×10^6	m^2/m^3
α_a	0.6	–
α_c	0.4	–
Electrolyte: $\sigma_i = \sigma_0 T^{-1}\exp(-E_a/RT)$		
Thickness	15	μm
σ_0	3.87×10^7	S/m
E_a	82.3	kJ/mol

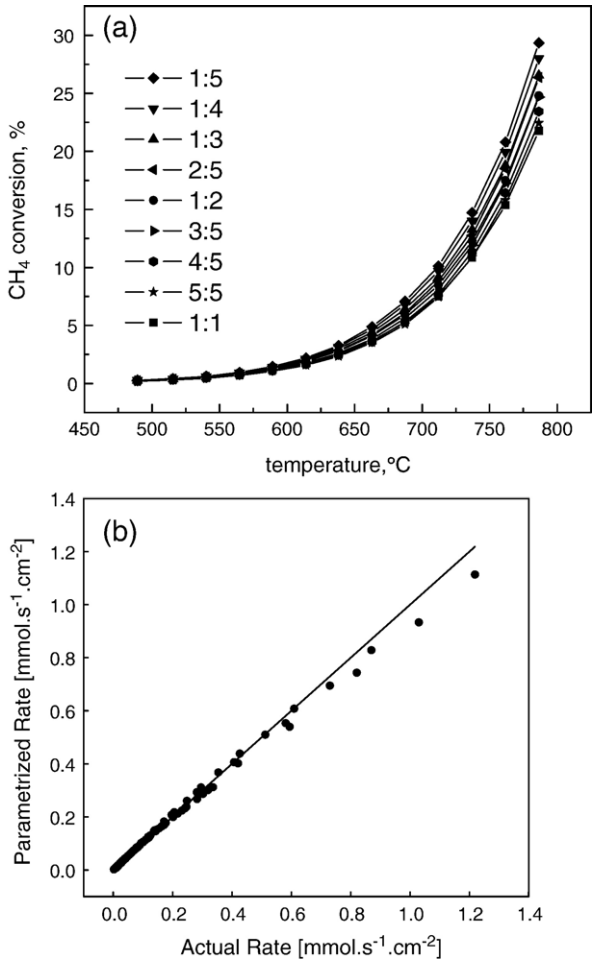

Fig. 3. Conversion of methane over $Ba_{0.5}Sr_{0.5}Co_{0.8}Fe_{0.2}O_{3-\delta}$ (BSCF). (a) Percentage conversion as a function of temperature for gas compositions as indicated in the legend (O_2 ml/min; CH_4 ml/min; balance He for a total flow rate of 130 ml/min); and (b) comparison of actual and calculated conversion rates (to CO_2) based on parameterization of conversion data, Eq. (7).

Non-zero concentrations of hydrogen and water are explicitly assigned at the inlet as part of the initial conditions to avoid singularities in the computation. Parameters used to describe the MEA structure are listed in Table 1. Under each set of conditions, the simulation is iterated until steady state is achieved.

4. Experiments for obtaining model parameters

4.1. Methane oxidation over BSCF

The catalytic properties of the BSCF cathode powder, prepared by a chemical solution method [5], were characterized using a conventional flow-through, tubular quartz reactor oriented vertically and with the flow directed downwards [6]. Measurements were performed using a fixed bed of 0.26 g of BSCF powder (specific surface area of 0.263 m^2/g as determined by BET methods) mixed with 1.2 g quartz powder. (The quartz powder was tested for catalytic inactivity prior to data collection.) The reactor feed (a mixture of methane, oxygen, and helium diluent) was maintained at a constant total flow rate of 130 sccm (standard cubic centimeters per minute). Nine reactant flow compositions were examined: with the methane flow rate fixed at 1 sccm, the oxygen flow rate was varied from 1 to 5 sccm (in 1 sccm steps) and with the oxygen flow rate fixed at 5 sccm, the methane flow rate was varied

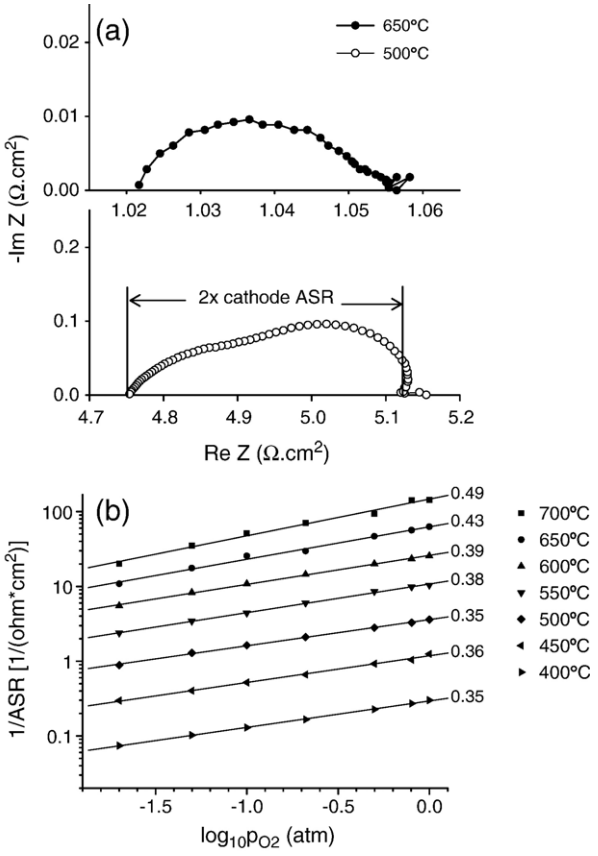

Fig. 4. Cathode polarization resistance of BSCF+SDC (70:30 wt.) | SDC | BSCF+SDC (70:30 wt.) symmetric cells. (a) Typical impedance spectra obtained under 0.2 atm p_{O_2} and at the temperatures indicated; and (b) summary of derived interfacial area specific resistances (ASRs) with value of temperature dependent exponent (Eq. (10)) as indicated.

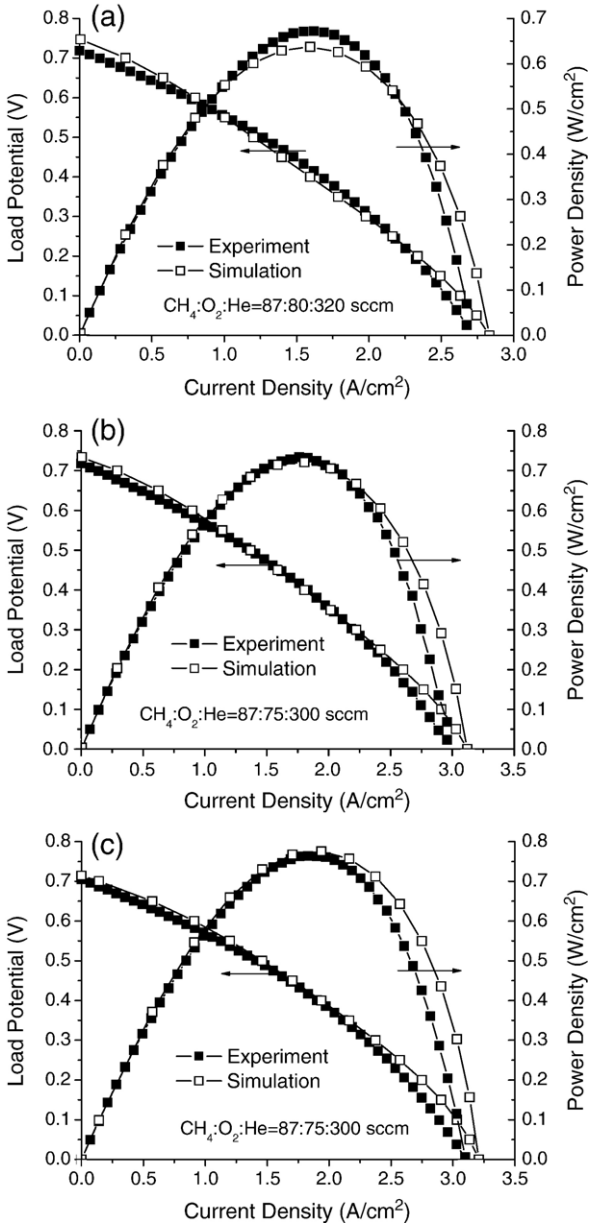

Fig. 5. Simulated vs. experimental polarization curves for CH_4, O_2 and He flow rates as indicated. (a) T_{furn}=600 °C, T_{cell}=743 °C; (b) T_{furn}=625 °C, T_{cell}=763 °C; and (c) T_{furn}=650 °C, T_{cell}=786 °C. Simulations performed isothermally using measured cell temperatures.

from 1 to 5 sccm (in 1 sccm steps). A high level of helium dilution was employed in order to minimize the total volumetric change upon reaction. At the beginning of each measurement, the BSCF sample was pre-treated for 5 h under a stoichiometric fuel:oxygen ratio (1:2) and at the highest test temperature (furnace set temperature of 775 °C), in order to stabilize catalytic activity. Reactor products were characterized using an in-line Varian CP-4900 Micro-GC, capable of detecting, in addition to hydrocarbons, CO, CO_2 and O_2. Hydrocarbon conversion at the outlet was determined by balancing the carbon in the product stream.

The percentage of the inlet methane consumed over BSCF as a function of (measured furnace) temperature is shown in Fig. 3a for the various gas compositions examined. Even at 785 °C, less than

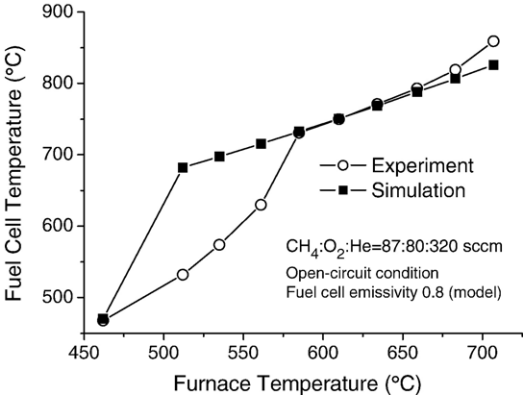

Fig. 6. Simulated and measured cell temperatures for the operational conditions indicated.

30% of the methane is consumed, reflecting the inactivity of BSCF for methane oxidation, and hence its value in SCFC operation. The carbon-bearing products were almost entirely CO_2, with less than 2% conversion to C_2H_4 and C_2H_6 at the highest temperatures, and undetectable levels of higher hydrocarbons or CO for all conditions.

The rate of conversion of methane to CO_2 (per unit BSCF surface area) was fit according to the expression

$$r = k \cdot P_{CH_4}^{m} \cdot P_{O_2}^{n} \tag{7}$$

where k is a rate constant with an Arrhenius temperature dependence, and the m and n exponents were found to be temperature independent. The suitability of this parametrization procedure is evident from the Fig. 3b, in which the measured and fitted conversion rates are compared.

4.2. Exchange current density

Complete characterization of an electrode material to establish the overpotential at the electrode–electrolyte interface requires measurement of current–voltage characteristics using a three-electrode configuration. A much simpler experiment involves the measurement of the interfacial area specific resistance (ASR) for an electrode | electrolyte | electrode cell (two-electrode) configuration. This quantity is related to the terms of the Butler-Volmer equation according to

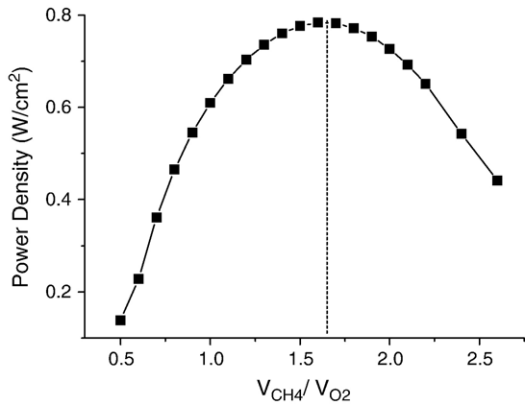

Fig. 7. Simulated power density at 0.4 V versus fuel-to-oxygen ratio at 750 °C.

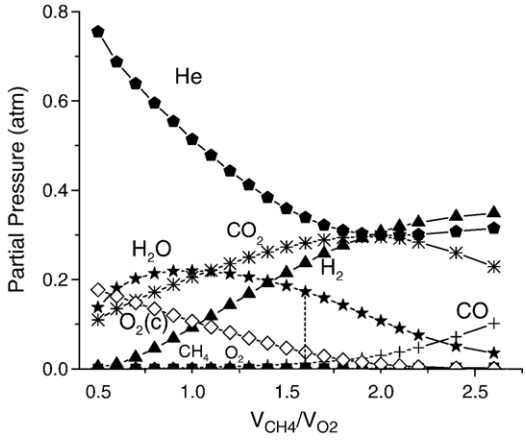

Fig. 8. Partial pressure of gas components at the anode–electrolyte interface and the O_2 concentration at cathode–electrolyte interface as functions of fuel-to-oxygen ratio at 750 °C.

$$\mathrm{ASR}^{-1} = \frac{\mathrm{d}i}{\mathrm{d}\eta}\Big|_{\eta=0} = i_0(\alpha_c + \alpha_a)\frac{F}{RT} \Rightarrow i_0 = \frac{RT \cdot \mathrm{ASR}^{-1}}{(\alpha_c + \alpha_a) \cdot F} \tag{8}$$

Note that in this formulation the number of electrons transferred during the reaction (often denoted as n) is implicitly included in the definition of the asymmetry factors, and that for charge transfer processes that include more than one step, even without the inclusion of n, the sum of the asymmetric factors can be greater than one [9]. Eq. (8) shows that measurement of the interfacial ASR does not completely define the exchange current density. However, the ASR data do yield i_0 within a constant factor, the sum of the asymmetry parameters. These terms were used as fitting parameters in simulating the fuel cell polarization data.

The interfacial ASR for the Ni-SDC | SDC interface was taken from the experimental data of Lai and Haile, measured from Pt | SDC | Pt symmetric cells under reducing conditions [16]. In that work, it was proposed that ceria itself is directly active for the electrochemical oxidation of hydrogen and thus the nature of the metal species should not affect electrocatalysis rates. The ASR was found to be dependent on oxygen partial pressure as well as temperature, according to

$$(\mathrm{ASR})^{-1} = (\mathrm{ASR}_0)^{-1} \exp\left(\frac{-E_{act}^{anode}}{k_b T}\right) P_{O_2}^{-1/4} \tag{9}$$

with $\mathrm{ASR}_0 = 8.13 \times 10^{-9}\ \Omega\ \mathrm{cm}^2\ \mathrm{atm}^{-1/4}$ and $E_{act}^{anode} = 2.67$ eV. Here, the oxygen partial pressure at the anode electrolyte interface is calculated from the equilibrium between H_2, O_2 and H_2O, where the hydrogen and water partial pressures are obtained from the porous electrode submodel.

The interfacial ASR for the BSCF-SDC | SDC interface was obtained in this work from impedance measurements of electrolyte-supported BSCF-SDC | SDC | BSCF-SDC symmetric cells under oxidizing conditions. Dense pellets of SDC (prepared from in-house synthesized ceria powder [6]) were obtained by

sintering at 1350 °C for 5 h. Onto these pellets thin (~10 μm) layers of BSCF+SDC (in a 70:30 weight ratio) composites were applied by colloidal spray deposition and the complete structure sintered at 1000 °C for 5 h under flowing nitrogen. Impedance data were collected at temperatures of 450 to 725 °C, and under oxygen partial pressures of 0.01 to 1 atm using a Solartron 1260 A Frequency response analyzer, over the frequency range 1 mHz to 10^5 Hz, and at a voltage amplitude of 20 mV.

Typical impedance spectra obtained from these measurements are presented in Fig. 4. Like the anode, the cathode interfacial resistance was found to depend on both temperature and oxygen partial pressure. In this case, however, the exponent in the pO_2 dependence also varied with temperature, yielding an overall expression

$$(\mathrm{ASR})^{-1} = (\mathrm{ASR}_0)^{-1} \exp\left(\frac{-E_{\mathrm{act}}^{\mathrm{cathode}}}{k_b T}\right) P_{O_2}^{\gamma(T)} \quad (10)$$

with $(\mathrm{ASR}_0)^{-1} = 1.35 \times 10^8\ \Omega^{-1}\ \mathrm{cm}^{-2}\ \mathrm{atm}^{-\gamma}$ and $E_{\mathrm{act}}^{\mathrm{cathode}} = 1.16$ eV, and $\gamma(T)$ being well-fit according to $\gamma(T) = \gamma_0 + \gamma_1 \exp(T/T_\gamma)$, where $\gamma_0 = 0.35$, $\gamma_1 = 3.43 \times 10^{-6}$, and $T_\gamma = 91.3$ K.

Other parameters that could not be (directly) measured from experiment were either estimated (e.g. porosity and pore size are estimated from SEM images) or left as free fitting parameters. This will be further discussed in the next section.

5. Results and discussion

5.1. Fuel cell performance

Three representative polarization curves (derived both from experiment and from simulation, the latter discussed below) are shown in Fig. 5. The polarization curve was obtained at a furnace set temperature of 600 °C, with flow rates of CH_4:O_2:He = 87:80:320 sccm, and the second and third at 625 and 650 °C, respectively, both with flow rates of CH_4:O_2:He = 87:75:300 sccm. Actual fuel cell temperatures were found to be 743, 763 and 786 °C, respectively, due to the exothermic reactions occurring in the anode. Temperature gradients along the stream-wise direction of the cell were typically 10–20 °C, with the leading edge being hotter than the downstream edge.

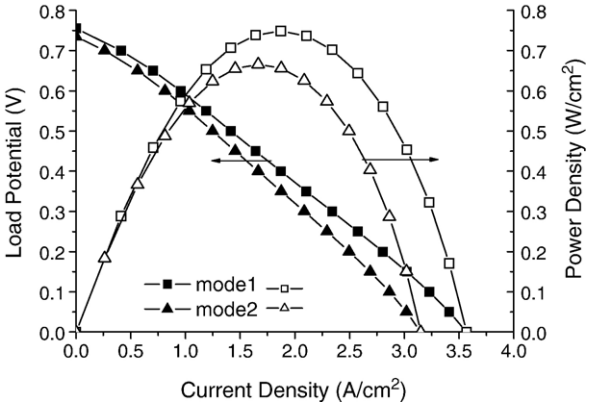

Fig. 9. Comparison of fuel cell polarization curves for cells placed in different orientations.

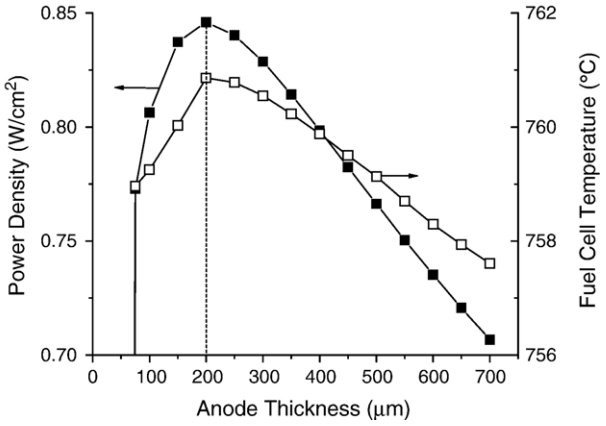

Fig. 10. Fuel cell power density at 0.4 V and 600 °C furnace temperature as a function of anode thickness.

The power densities achieved here, peak values of 670–760 mW/cm^2 for the three measurements shown, are the highest reported in the literature to date for single chamber fuel cells. This is attributed, in large part, to the excellent oxygen electro-reduction activity of the BSCF cathode (Fig. 3), combined with its inactivity towards alkane chemical oxidation (Fig. 2). In addition, the fuel mixture is somewhat fuel rich relative to the 1:1 methane: oxygen mixtures utilized in other laboratories. As described below, the fuel cell power output is highly sensitive to the fuel to oxygen ratio.

The large difference between the furnace set temperature of actual cell temperature is consistent with our previous results for propane fueled SCFCs and with other results in the literature and indicates the importance of knowledge of the true cell temperature in understanding SCFC behavior. However, for the relatively small diameter fuel cells used here (1.33 cm) the gradient along the cell is sufficiently slight that one can refer to the average cell temperature to represent the entire structure.

5.2. Model calibration and validation

The experimental data-set obtained at a furnace temperature of 600 °C were used to calibrate the model, using an isothermal simulation in which the cell temperature was fixed at the measured value of 743 °C. Adjusted parameters were the asymmetry factors (Eq. 4) of the anode and cathode electrochemical reactions. Because heat transfer aspects are not included in the isothermal simulation, values for the emissivity and thermal conductivity were not necessary at this stage. The identical set of parameters were then used to simulate the polarization curves corresponding to the other two sets of conditions, again, isothermally, using the actual (measured) cell temperatures. As Fig. 5 indicates, there is excellent agreement between the experimental data and the simulations, validating the overall approach and giving confidence in the accuracy of the model for performance predictions.

The emissivity and thermal conductivity (both averaged for the entire fuel cell structure) were then obtained by fitting the

temperature rise and streamwise temperature gradient across the cell to the experimental data obtained for a selected fuel cell experiment. From the fit at this single condition, the temperature rises observed for different furnace set temperatures were well-simulated (Fig. 6), indicating the appropriateness of the derived material parameters (emissivity = 0.8 and thermal conductivity = 30 W/m/K).

5.3. Model predictions

The following examples will show the application of the model to predict cell performance under various operation conditions and to help improve system design. First, we study the dependence of power density on fuel-to-oxygen ratio, an important parameter. The ratio of methane to oxygen flow rates is varied from 0.5 to 2.0. Temperature is 750 °C isothermal, and load potential is fixed at 0.4 V. The simulation result is shown in Fig. 7. The optimum ratio is found to be 1.65. Fig. 8 shows the partial pressures of all the gas-phase species at the anode–electrolyte interface, together with oxygen partial pressure at the cathode–electrolyte interface at the middle point of the cell along the streamwise direction. Since hydrogen and oxygen are the two reactants for electrochemistry at the anode and cathode, respectively (note the low CO concentrations at all fuel-to-oxygen ratios indicating the relative insignificance of this species to the overall electrochemistry), the peak power density should occur where both reactants are present in sufficient concentrations. From Eqs. (1) and (2), the current density at fixed E will increase if p_{H_2} or p_{O_2} is increased, and decrease if p_{H_2O} increases. As shown in Fig. 8, if the fuel/oxygen ratio is close to stoichiometric (0.5), very little hydrogen is produced, and therefore the current and power are very low. In this regime, the anode chemistry is principally catalytic combustion, producing H_2O and CO_2 by non-electrochemical routes. In the opposite (fuel rich) limit, ample hydrogen is produced by partial oxidation on the anode side, but oxygen is depleted by parasitic catalytic combustion on the cathode side. At intermediate fuel/oxygen ratios, adequate hydrogen is produced in the anode, while sufficient oxygen is still present on the cathode side. The precise value of the optimal fuel/oxygen ratio for maximum power output must depend, amongst other factors, on the electrocatalytic activity of the anode and cathode catalysts. The extraordinary properties of the BSCF cathode (low activity for hydrocarbon oxidation combined with high activity for electrochemical oxygen reduction) are likely responsible for the occurrence of the fuel/air ratio for maximum power at a value shifted towards rather fuel rich mixtures (because a higher hydrogen partial pressure in the vicinity of the anode–electrolyte interface is required in order for the anode electrochemistry to keep pace with that of the cathode). While systematic studies to probe this hypothesis have not been carried out, such an interpretation can also explain the observation that the optimal fuel:O_2 ratio for propane-fueled SCFCs is ~3:1 for ceria based fuel cells incorporating $Sm_{0.5}Sr_{0.5}CoO_{3-\delta}$ (SSC) as the cathode [6], whereas as it is ~2:1 for the type of cells employed here [5]. The complete system implications for operation under fuel rich conditions have yet to be considered, but may have the benefit of reducing the total volume of gas processed, and thus the size and weight of the associated hardware. One also anticipates that operation under fuel rich conditions results in a smaller temperature rise at the cell as insufficient oxygen is available for the generation of deep oxidation products and the associated heat release.

Second, we evaluate the influence of flow geometry on fuel cell performance. In particular, we examine the influence of rotating the cell such that it is oriented perpendicular to the gas flow direction (with a reduced diameter of 5.29 mm). We define modes 1 and 2 to refer to orientations in which the cathode and anode are, respectively, exposed to the fresh gas mixture. Polarization curves are computed with flow rates of CH_4:O_2:He = 87:75:300 sccm and an isothermal temperature of 750 °C (Fig. 9). The simulations reveal that the peak power density of mode 1 is substantially (12%) greater than that of mode 2. An investigation of the partial pressures of gas-phase species within the electrodes shows that the improvement in power is due to the higher oxygen partial pressure at the cathode–electrolyte interface. Specifically, the interfacial oxygen pressure of mode 1 is twice that of mode 2. The latter is lower not only because oxygen is consumed by the anode prior to its arrival at the cathode, but also because the partial oxidation products (H_2 and CO) generated by the anode are transported in the gas phase (via both convection and diffusion) to the cathode. There, they consume additional oxygen through their full oxidation over the cathode catalyst surface. The result is consistent with the observations of Stefan et al. [17] who reported higher power densities from propane–air SCFCs for cells oriented with the cathode exposed to the fresh gas than from those with the anode in this position. Overall, it is apparent that enhanced performance can be obtained by optimizing flow geometry, even in the absence of modifications to the fuel cell component materials or dimensions.

A key fuel cell parameter amenable to variation (and not yet systematically studied in the experimental literature) is the anode thickness. Because the anode plays such a critical role in SCFC operation it can be anticipated that fuel cell power output would be sensitive to the anode dimensions. Fig. 10 shows the power density as a function of anode thickness at a fixed load potential of 0.4 V (which approximately corresponds to the voltage at peak power). The gas flow rate is CH_4:O_2:He = 87:75:300 sccm. Because the anode dimensions will influence the heat and cell temperature rise, the simulation was performed non-isothermally with a furnace temperature of 600 °C. The actual (computed) cell temperature is also shown in the figure.

In the present experimental configuration, the anode thickness is fixed at 700 μm. The simulation results indicate that the power output is indeed highly sensitive to the anode dimensions. While the maximum in power output may not occur exactly at 200 μm as suggested by the simulation, it is clear that reducing the anode thickness from its present value will improve performance. The cell temperature has a similar dependence on anode thickness, peaking in this case at 200 μm too. The computed gas compositions (data not shown) reveal that hydrogen production occurs preferentially at the exterior surface of the anode, and that for thicker anodes, the maximum hydrogen concentration is high due to the abundance of partial oxidation reaction sites. However, the hydrogen concentration at the electrolyte–anode interface is higher for thinner anodes

because of the shorter diffusion path, leading to better performance for thin anodes. When the anode thickness is lowered beyond a critical value, the loss of catalytic sites begins to have a detrimental effect, reflected also in the dramatic decrease in cell temperature. These effects combine to produce the thickness dependence of power output evident in Fig. 10.

6. Conclusions

Single-chamber fuel cells have significant potential, particularly for applications in which the simplicity of a single gas channel and absence of seals is of paramount importance. We have demonstrated that very useful power densities may be achieved, and this may be done at relatively low operating temperatures, making thermally self-sustaining operation possible. However, to realize their full potential, it is necessary to determine optimal catalysts, electrode microstructures, geometries, flow configurations, etc. As a significant step toward this goal, we have described here the development and experimental validation/calibration of a quantitative, physically-based model of an SCFC that captures the most important chemical, electrochemical, and physical processes responsible for SCFC operation. The approach described here, in which simulation and experiment are used together, provides a firm basis for both developing mechanistic understanding and optimizing SCFC stack designs.

Acknowledgment

This work was supported by the DoD Defense Advanced Research Projects Agency (DARPA) within the Integrated Micropower Generator (IMG) program under grant N66001-01-1-8966. We greatly appreciate the constructive suggestions of Dr. Carlos Pantano.

References

[1] T. Hibino, A. Hashimoto, T. Inoue, J. Tokuno, S. Yoshida, M. Sano, Science 288 (2000) 2031.
[2] T. Hibino, A. Hashimoto, M. Yano, M. Suzuki, S. Yoshida, M. Sano, J. Electrochem. Soc. 149 (2) (2002) A133.
[3] Z. Shao, S.M. Haile, J. Ahn, P.D. Ronney, Z. Zhan, S.A. Barnett, Nature 435 (2005) 795.
[4] T. Suzuki, P. Jasinski, V. Petrovsky, H.U. Anderson, F. Dogan, J. Electrochem. Soc. 152 (3) (2005) A527.
[5] Z. Shao, S.M. Haile, Nature 431 (2004) 170.
[6] Z. Shao, C. Kwak, S.M. Haile, Solid State Ionics 175 (2004) 39.
[7] Y. Hao, C. Pantano, D.G. Goodwin, Proceedings of the Ninth International Symposium on Solid Oxide Fuel Cells (SOFC IX), Quebec City, Canada, 2005.
[8] E.A. Mason, A.P. Malinauskas, Gas Transport in Porous Media: the Dusty-Gas Model, American Elsevier, New York, 1983.
[9] H. Zhu, R.J. Kee, V.M. Janardhanan, O. Deutschmann, D.G. Goodwin, J. Electrochem. Soc. 152 (12) (2005) A2427.
[10] T. Hibino, A. Hashimoto, T. Inoue, J. Tokuno, S. Yoshida, M. Sano, J. Electrochem. Soc. 148 (6) (2001) A544.
[11] T. Suzuki, P. Jasinski, V. Petrovsky, H.U. Anderson, F. Dogan, J. Electrochem. Soc. 151 (9) (2004) A1473.
[12] I. Riess, Solid State Ionics 157 (2003) 1.
[13] I. Riess, J. Phys. Chem. Solids 47 (2) (1986) 129.
[14] I. Riess, M. Gödickemeier, L.J. Gauckler, Solid State Ionics 90 (1996) 91.
[15] M. Gödickemeier, L.J. Gauckler, J. Electrochem. Soc. 145 (2) (1998) 414.
[16] W. Lai, S.M. Haile, J. Am. Ceram. Soc. 88 (11) (2005) 2979.
[17] I.C. Stefan, C.P. Jacobson, S.J. Visco, L.C. De Jonghe, Electrochem. Solid-State Lett. 7 (7) (2004) A198.